Atmospheric Research 332 (2026) 108701

Contents lists available at ScienceDirect

Atmospheric Research

journal homepage: www.elsevier.com/locate/atmosres

Estimating the full-day planetary boundary layer height from lidar, AMDAR, and radiosonde observations over Beijing, China

Jieyu Hou [a], Mengyao Li [b], Guicai Ning [b,c,*], Tianwen Wei [b], Jinlong Yuan [b], Haiyun Xia [b,d,*]

[a] Reading Academy, Nanjing University of Information Science and Technology, Nanjing 210044, China
[b] Collaborative Innovation Centre on Forecast and Evaluation of Meteorological Disasters, School of Atmospheric Physics, Nanjing University of Information Science and Technology, Nanjing 210044, China
[c] Chengdu Plain Urban Meteorology and Environment Observation and Research Station of Sichuan Province, School of Atmospheric Sciences, Chengdu University of Information Technology, Chengdu 610225, China
[d] School of Earth and Space Science, University of Science and Technology of China, Hefei 230026, China

ARTICLE INFO

Keywords:
Planetary boundary layer height
Lidar
AMDAR
Integrated full-day observations

ABSTRACT

The planetary boundary layer (PBL) is the core transition zone for mass, energy, and momentum exchanges between surface and free atmosphere, significantly modulating weather, climate and human activities. However, full-day evolutions of PBL structure and PBL height (PBLH) remain limited as insufficient atmospheric vertical observations. Here, we comprehensively evaluate PBL features and PBLH detected from radiosonde, AMDAR, and lidar over Beijing, China. The PBL detections from the three platforms are significantly consistent, confirming their collective efficacy in full-day PBL monitoring. Notably, some outlies with obvious discrepancies in PBLH detection among these three platforms are extracted and their underlying causes are revealed. Then, these outliers are removed and the consistency in PBLH detected from the three platforms markedly improved. The correlation coefficient (R) and the root mean square error (RMSE) in PBLH detected from radiosonde and AMDAR range from 0.44 to 0.64 and 207.02 m to 264.85 m, respectively. PBLH detected from radiosonde (AMDAR) and lidar under stable (convective) and neutral thermal conditions significantly correlates at R ranging from 0.53 (0.67) to 0.67 (0.73) and RMSE from 218.77 m (324.77 m) to 304.23 m (386.57 m). Moreover, PBLH detections from all three platforms consistently show that convective PBLH > neutral PBLH > stable PBLH. These results highlight the reliability of aircrafts' and lidar's observations in detecting PBLH and PBL thermal structures. Finally, PBL detections from the three platforms are integrated to monitor full-day PBL, compensating for the radiosonde's limitation in monitoring convective boundary layer.

1. Introduction

The Planetary Boundary Layer (PBL), as the core transition zone for the exchange of matter, energy, and momentum between the underlying surface and the free atmosphere, typically has a vertical extent of several hundred meters to a few kilometers and plays a crucial regulatory role in weather, climate, and environmental processes (Stull, 1988). Simultaneously, the PBL encompasses the space where human activities occur, and meteorological and environmental changes within it directly affect human survival and development (Quan et al., 2013; Zilitinkevich, 2012). Therefore, research on the PBL has consistently been a focal point and frontier in the fields of atmospheric and environmental sciences. Particularly, since China implemented its low-altitude airspace opening policy in 2014, flight activities within the PBL below 1000 m have increased significantly (Fan et al., 2017), propelling the refinement of the PBL research into a new phase.

To ensure low-altitude flight safety, "National Airspace Basic Classification Method" of China stipulates that aircraft operating below 3000 m must maintain a horizontal distance of at least 1500 m from clouds and visibility of no less than 5 km (Civil Aviation Administration of China, 2023, https://www.caac.gov.cn/XXGK/XXGK/TZTG/202312/t20231221_222397.html). As a key parameter in PBL research, the planetary boundary layer height (PBLH) is a primary characteristic variable for determining turbulent mixing, vertical disturbances, convective transport, cloud bands, and atmospheric visibility, with significant impacts on the development and evolution of clouds, convection, and atmospheric pollution (Garratt, 1994; Yin et al., 2019). For instance, the PBLH can measure the retention and dispersion capacity of

* Corresponding authors.
E-mail addresses: guicaining@nuist.edu.cn (G. Ning), hsia@ustc.edu.cn (H. Xia).

https://doi.org/10.1016/j.atmosres.2025.108701
Received 26 August 2025; Received in revised form 20 November 2025; Accepted 10 December 2025
Available online 11 December 2025

atmospheric pollutants, as well as the vertical transport efficiency of atmospheric heat and water vapor, which are crucial for cloud and fog macro-microphysical processes (Miao and Liu, 2019; Shao et al., 2023). Consequently, accurately determining the PBLH and conducting detailed research on it contributes to enhancing our understanding of atmospheric pollution and cloud-fog formation and dissipation processes, thereby improving forecasting and early warning capabilities for low-altitude visibility and low cloud conditions, which holds significant importance for the safe development of the low-altitude economy.

Currently, there are primarily three platforms for detecting PBLH, including radiosonde, lidar, and aircraft measurements (Chen et al., 2022; Guo et al., 2016; Wang et al., 2025; Seidel et al., 2012; Rahn and Mitchell, 2016; Zhang et al., 2020b). Among them, radiosonde measurements provide high-precision vertical profiles of temperature, humidity, and pressure to retrieve PBLH. However, radiosonde observations are fixed at 00:00 and 12:00 UTC, typically unable to provide information on daytime convective boundary layers over China (Seidel et al., 2010). In contrast, Coherent Doppler Wind Lidar (CDWL) retrieves high temporal resolution PBLH by tracers such as turbulent kinetic energy dissipation rate (TKEDR) and carrier-to-noise ratio (CNR) (Wang et al., 2021). However, cloud interference, strong wind shear, and non-uniform aerosol distribution could reduce the reliability of CDWL data, posing challenges to the accurate determination of PBLH (Milroy et al., 2012; Zhong et al., 2020). In addition, Aircraft Meteorological Data Relay (AMDAR) from real-time collections by aircrafts can be used to supplement observational gaps of PBLH during daytime. However, the capability for long-term continuous observation is limited as flight routes distribution and insufficient nighttime observations (Zhang et al., 2019; Doerenbecher and Mahfouf, 2019). Overall, all three platforms can detect PBLH, but their results demonstrate certain differences and limitations (Zhang et al., 2020a). Moreover, most of existing studies focus on estimating PBL features retrieved from only two observational platforms, such as AMDAR versus radiosonde (Ding et al., 2015; Zhang et al., 2019; Xu et al., 2022), AMDAR versus lidar (Ng and Hon, 2022; Ayazpour et al., 2023), or lidar versus radiosonde (Cooper and Eichinger, 1994; Zhang et al., 2016; Su et al., 2020), while a concurrent evaluation of the three platforms is rare and limits our understanding of full-day PBL. Thus, comprehensively evaluating these three platforms in observing PBLH is urgently needed to meticulously characterize full-day PBL and provide significant implications for enhancing aviation meteorological support capabilities.

Given that Beijing, an international metropolis, offers simultaneous radiosonde, lidar, and AMDAR observations and poses substantial potential for low-altitude economic development, we thus take Beijing as an example to detect the PBLH from these three observational platforms and evaluate the accuracy and consistency of each platform's detection. Simultaneously, the PBLH data from all three platforms are integrated to construct a more continuous and reliable full-day dataset, providing essential support for low-altitude economic meteorological services. The second section introduces the sources of the three data types observed by the three platforms and the corresponding three methods for retrieving PBLH. The third section presents a comprehensive analysis, comparison, and evaluation of PBLH retrieved by different detection platforms and the corresponding methods. The fourth section provides the main conclusions and prospects for future research.

2. Data and methods

2.1. Data and instruments

2.1.1. Radiosonde observations

The radiosonde dataset used in this study is obtained from the University of Wyoming Atmospheric Science Radiosonde Archive (https://weather.uwyo.edu/upperair/sounding.html), which provides atmospheric profiles of temperature, horizontal wind vectors, relative humidity, and potential temperature at 08:00 and 20:00 Beijing Time (BJT). We select sounding profiles from the Beijing station (see the blue triangle in Fig. 1) covering the period from 1 January to 31 December 2022 to retrieve PBLH. To ensure retrieval accuracy, only profiles with at least seven valid vertical levels below 5000 m are retained (Zhang et al., 2013).

2.1.2. Coherent Doppler wind lidar observations

Vertical measurements from a coherent Doppler wind lidar (CDWL; hereafter referred to as "lidar") are employed for the period from 13 April to 31 December 2022. The lidar was deployed at the Institute of Software, Chinese Academy of Sciences (39.98°N, 116.34°E, see the red star in Fig. 1), Beijing, China. It provides measurements of wind speed, CNR, and other meteorological variables. The key parameters of the lidar are listed in Wang et al. (2024b). To enhance data reliability and minimize noise and small-scale fluctuations, TKEDR values with wind error > 0.5 are removed. Additionally, a spatial smoothing with a 250 m moving average and a temporal smoothing with a 7-min moving average are applied to the TKEDR data.

Notably, the timestamps of radiosonde and AMDAR observations are available only at hourly resolution, while lidar observations are refined to the second level. Thus, the PBLH detected from lidar are further temporally matched to hourly time points to ensure its temporal consistency with the radiosonde and AMDAR. Specifically, lidar-derived PBLH values closest to each full hour are extracted and compared with the PBLH measurements from radiosonde and AMDAR observations at that hour. If the closest observations of lidar are invalid, the nearest valid PBLH values within 30 min before and after this full hour are selected. If no valid lidar observations are available within this window, the PBLH for that hour is recorded as missing. Given that radiosonde observations are fixed at 00:00 and 12:00 UTC, the valid observations of AMDAR and lidar at these two hours are used to conduct the comparisons of detected PBLH between AMDAR and radiosonde or lidar and radiosonde.

2.1.3. Aircraft meteorological data relay (AMDAR)

The Aircraft Meteorological Data Relay (AMDAR) system provides automated, in-flight meteorological reports from commercial aircraft worldwide. These hourly observations include geographic coordinates, altitude, wind speed and direction, turbulence, and temperature. In this study, two AMDAR data sources are utilized. One is provided by the Meteorological Assimilation Data Ingest System (https://madis-data.cprk.ncep.noaa.gov/madisPublic1/data/archive/) and another is provided by the UK Met Office MetDB system (https://catalogue.ceda.ac.uk/uuid/33f44351f9ceb09c495b8cef74860726/). The two datasets are merged based on timestamp for the period from 1 January to 31 December 2022, followed by a quality control procedure. To ensure the reliability of the PBLH retrievals, we retain only those profiles with altitudes below 1800 m, which is based on the finding by Wang et al. (2008) i.e., the PBLH over Beijing typically $\leq$1800 m. Additionally, only data within 50 km of Beijing Daxing International Airport (see the orange circle in Fig. 1) are considered, and profiles are excluded if they have no data below 500 m or had fewer than four data points below 1000 m. Corresponding surface meteorological data are also collected from the Integrated Surface Database (ISD) provided by the National Oceanic and Atmospheric Administration (https://www.ncei.noaa.gov/metadata/geoportal/rest/metadata/item/gov.noaa.ncdc:C00532/html#). Potential temperature is calculated from temperature and pressure data to construct vertical potential temperature profiles. Additional quality control is applied to remove redundant or anomalous profiles, with details shown below. When multiple aircraft report observations simultaneously, resulting in more than one vertical profile, only a single representative profile is retained (Fig. S1a); outlier values are manually removed (Fig. S1b); when data for a given time are too disordered or inconsistent to be corrected using the above procedures, the entire profile is discarded (see Fig. S1c).

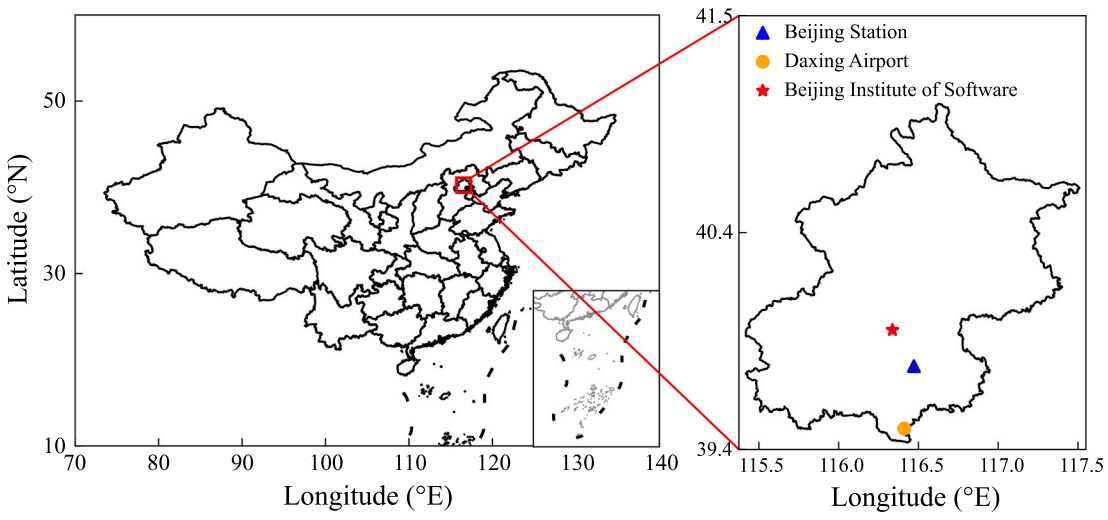

Fig. 1. Study area and location of the Beijing station (blue triangle), Beijing Daxing International Airport (orange circle), and the Doppler wind lidar system (red star). (For interpretation of the references to colour in this figure legend, the reader is referred to the web version of this article.)

2.2. PBLH retrieval based on radiosonde and AMDAR data

2.2.1. Potential temperature profile method

The PBL exhibits distinct structural regimes over the diurnal cycle, typically categorized into three types: stable boundary layer (SBL), neutral boundary layer (NBL), and convective boundary layer (CBL) (Stull, 1988). Representative examples of these boundary layer types are shown in Fig. S2. Generally, SBLs occur at night or in the early morning, CBLs dominate during daytime, and NBLs may appear at any time of the day. As each type requires a specific approach for PBLH determination, identifying the boundary layer type is a precondition. The classification approach involves calculating the potential temperature gradient $\Delta\theta/\Delta z$ between two levels closest to 50 m and 200 m above ground level. If $\Delta\theta/\Delta z > 1/150\ K \bullet m^{-1}$, the layer is classified as SBL; if $\Delta\theta/\Delta z < -1/150\ K \bullet m^{-1}$, it is considered as CBL; otherwise, it is categorized as NBL (Liu and Liang, 2010). For SBLs, the PBL height is defined as the top of the temperature inversion or the altitude with the minimum potential temperature gradient. In NBLs, the PBL height corresponds to the first level where the gradient exceeds 4 $K{\cdot}km^{-1}$. For CBLs, the PBL height is determined by the level where the gradient surpasses 4 $K{\cdot}km^{-1}$ and the potential temperature at that level is greater than the surface value (Sun, 2023).

2.2.2. Bulk Richardson number method

The bulk Richardson number method is a fundamental approach widely applied in climatological studies to estimate the PBLH (Hanna, 1969; Zilitinkevich and Baklanov, 2002; Zhang et al., 2014; Guo et al., 2016). The formula to calculate the Richardson number R_{ib} is:

$$R_{ib}(z) = \frac{\left(\frac{g}{\theta_{v0}}\right)\cdot(\theta_{vz} - \theta_{v0})\cdot z}{{u_z}^2 + {v_z}^2} \tag{1}$$

where g is the gravitational acceleration, taken as 9.8 $m \bullet s^{-1}$; θ_{vz} and θ_{v0} are the virtual potential temperatures at height z and at the surface, respectively; z is the height; ${u_z}^2$ and ${v_z}^2$are the squared zonal and meridional wind components at height z, respectively (Richardson et al., 2013). Due to the limited availability of humidity measurements in the AMDAR archive, potential temperature is used as a proxy for virtual potential temperature in Eq. (1) (Zhang et al., 2020b). Following the methodology proposed by Seidel et al. (2012), the threshold value of R_{ib} is set to 0.25. The PBLH is then defined as the lowest altitude where the Richardson number first exceeds this critical threshold.

2.3. PBLH Retrieval based on lidar data

Various techniques have been developed for retrieving PBLH from lidar observations, including visual inspection, gradient methods, wavelet transform, and threshold-based approaches. Among these, the threshold method based on turbulence intensity has gained wide adoption in recent studies due to its objectivity, simplicity, and operational efficiency (Wang, 2022; Su et al., 2024). In this study, the TKEDR value is used as an indicator of vertical variations in turbulence intensity. According to Smalikho and Banakh (2017), the formula to calculate TKEDR is:

$$TKEDR = \left[\frac{\overline{D_L}(\varphi_l) - \overline{D_L}(\varphi_1)}{A(l\Delta y_k) - A(\Delta y_k)}\right]^{\frac{3}{2}} \tag{2}$$

where $\overline{D_L}(\varphi_l)$ is the azimuth structure function; $A(y)$ is the theoretical calculation function; $\Delta y_k = \Delta\theta R_k cos\,\varphi$ ($\Delta\theta$ is in radians), with $l \geq 2$. The PBLH is defined as the first altitude at which TKEDR falls below $10^{-4}\ m^2 \bullet s^{-3}$ (Banakh et al., 2021; Wang, 2022; Wang et al., 2024a). The illustrative examples are provided in Fig. S3.

2.4. Methodological comparison

Notably, the considerations of PBL thermal and dynamic structures in retrieving PBLH are significantly different among the above three methods. In the case of the potential temperature profile method, the PBLH is determined by the vertical gradients of potential temperature, which highly relies on the thermal structure of PBL but does not account for the dynamic structure (Zhang et al., 2020a). As a result, we can retrieve PBLH solely from the potential temperature profile, but significant errors may arise under the weather conditions with strong wind shear or turbulence. In contrast, the bulk Richardson number method offers a more comprehensive determination of the PBLH by considering both thermal and dynamic PBL structure. However, its applicability is limited as the calculation of Richardson number is highly sensitive to the vertical resolution and accuracy of both potential temperature and horizontal wind observations (Zhang et al., 2020a). Compared with the above two methods, the TKEDR-based threshold method retrieves PBLH solely from the dynamic structure of PBL and the cloud interference, strong wind shear, and non-uniform aerosol distribution could reduce the reliability of the detected PBLH (Milroy et al., 2012; Zhong et al., 2020).

3. Results

This study compares the PBLH retrieved from three observational platforms: radiosonde, AMDAR, and lidar. Two retrieval methods, i.e., the potential temperature profile method and the bulk Richardson number method, are applied to both radiosonde and AMDAR data to estimate PBLH. Given the high temporal resolution and large volume of coherent Doppler wind lidar data, the lidar results are further compared with those from radiosonde and AMDAR observations under different boundary layer types. Specifically, the boundary layer is categorized into stable boundary layer (SBL), neutral boundary layer (NBL), and convective boundary layer (CBL), and the PBLH retrieval consistency is investigated for each category in detail.

3.1. Comparison of PBLH retrievals from radiosonde and AMDAR data

Given that both radiosonde and AMDAR observational platforms can observe both thermal and dynamic structures of PBL, both of the potential temperature profile method and the bulk Richardson number method are respectively selected to retrieve PBLH and the retrieved results are compared between the two observational platforms. In the case of the potential temperature profile method, the derived PBLH values from both radiosonde and AMDAR observations are compared. As shown in Fig. 2a and Fig. S4a, the correlation coefficient (R) between the two datasets is 0.29 with P value <0.1, and the root mean square error (RMSE) is 349.67 m, indicating weak overall correlation and limited statistical significance. As the observations of radiosonde are only available at 08:00 and 20:00 (BJT), the corresponding PBL is typically in a stable condition (SBL), where the consistency of PBLH derived from radiosonde is generally low (Wang et al., 2016; Su et al., 2020; Li et al., 2021). Further analysis reveals several outlier cases where the difference between the two datasets is obvious (e.g., one dataset reports PBLH >1000 m, while the other <500 m), which are marked with triangles in Fig. 2a. To elucidate the obvious discrepancies, the potential temperature profiles observed by radiosonde and AMDAR corresponded to the three triangle-marked are investigated and shown in Fig. S5. Based on the potential temperature profiles, we find that the atmospheric stability in the lower troposphere captured by AMDAR is much stronger than that from radiosonde, yielding much lower PBLH (Canché-Cab et al., 2024). After removing these obviously deviating points (marked by triangles in Fig. 2a), the consistency between the two observational platforms improves markedly, with the correlation coefficient increasing to 0.64 and the RMSE decreasing to 207.02 m, as shown in Fig. 2b and Fig. S4a, alongside a substantial improvement in statistical significance. The mean PBLH value detected from radiosonde is 274 m, whereas that detected from AMDAR is 340 m, indicating that the radiosonde's observations of PBLH tend to be lower.

When using the bulk Richardson number method to retrieve PBLH, the correlation between the two datasets remains low (Fig. 3 and Fig. S4f) and is highly consistent with the result derived from the method of potential temperature profiles (Fig. 2 and Fig. S4a). In addition to the triangle-marked outliers, another type of large discrepancy is observed (marked by stars in Fig. 3a), where one dataset reports PBLH >500 m and the other <100 m. To elucidate the two types' obvious discrepancy, the potential temperature profiles observed by radiosonde and AMDAR corresponded to the three triangle-marked and star-marked are investigated and shown in Fig. S6. Based on the potential temperature profiles, we identify two distinct sources of the observed discrepancies. One source is the sparse valid AMDAR potential temperature observations in the lower troposphere (Fig. S6a), which result in abnormally high PBLH retrieval. Moreover, the additional inclusion of surface station observations from the ISD introduces inconsistencies, as the near-surface potential temperature differs considerably from that obtained by the aircraft (Fig. S6b and Fig. S6c), thereby affecting the determination of PBLH. After excluding the abnormal data points, the correlation coefficient increases to 0.44 with P value <0.01 and the RMSE decreases to 264.85 m, as shown in Fig. 3b and Fig. S4f, reflecting a moderate improvement in agreement. The mean PBLH value detected from radiosonde is 189 m, whereas that detected from AMDAR is 265 m. The radiosonde's observations of PBLH are also lower than AMDAR.

Further comparison between the two retrieval methods indicates that the potential temperature profile method yields better overall consistency than the bulk Richardson number method (Fig. 2 and Fig. 3). This is likely because wind speed in the lower PBL varies sharply with height, and the bulk Richardson number method is highly dependent on accurate and high-resolution wind observations (Zhang et al., 2020a). In contrast, the potential temperature profile method primarily relies on thermal structure, making it less sensitive to vertical data density and accuracy, and thus more adaptable under limited observational conditions. Overall, the AMDAR-derived PBLH shows high agreement with radiosonde observations after outlier removal, indicating that AMDAR observations can effectively characterize both thermodynamic and dynamic structures of the PBL.

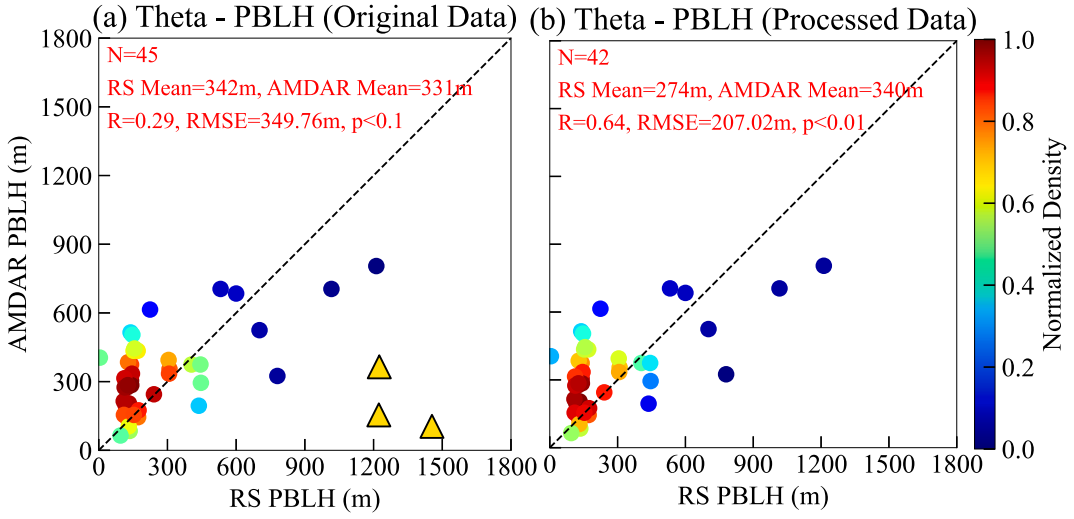

Fig. 2. Comparison of PBLH detected from radiosonde and AMDAR data (retrieved by the potential temperature profile method). The triangular markers indicate cases where one platform detected a PBLH >1000 m, while the other detected a PBLH <500 m.

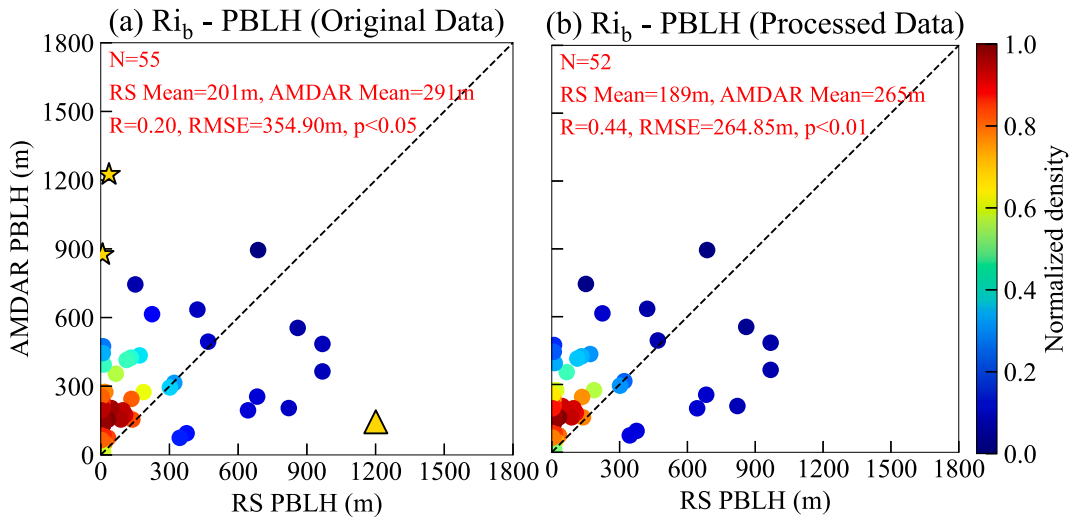

Fig. 3. Comparison of PBLH detected from radiosonde and AMDAR data (retrieved by the bulk Richardson number method). The triangular markers indicate cases where one platform detected a PBLH >1000 m, while the other detected a PBLH <500 m. The star-shaped markers indicate cases where one platform detected a PBLH >500 m, while the other detected a PBLH <100 m.

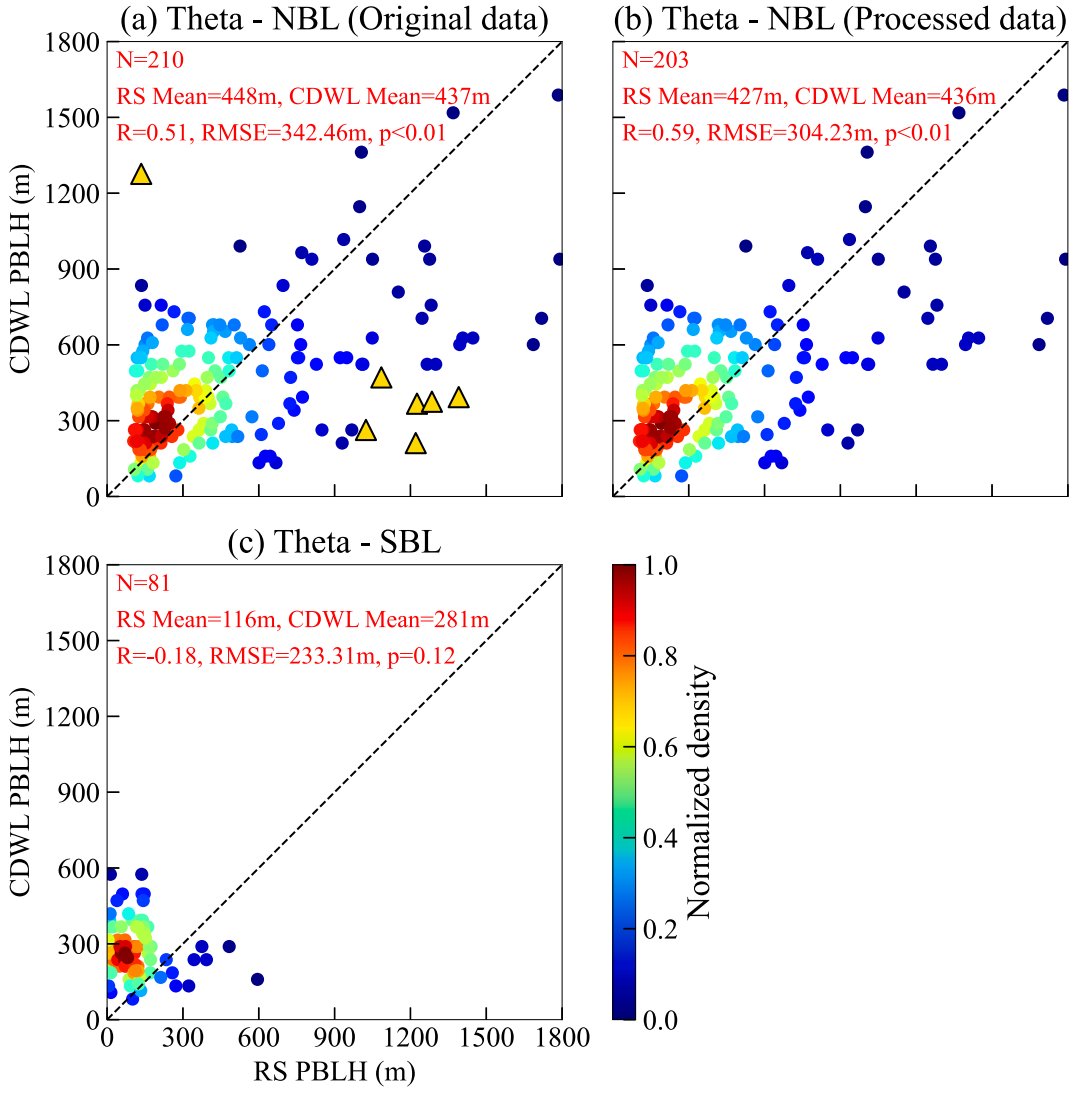

Fig. 4. Comparison of PBLH detected from radiosonde (retrieved by the potential temperature profile method) and lidar data (retrieved by the TKEDR-based threshold method). The triangular markers indicate cases where one platform detected a PBLH >1000 m, while the other detected a PBLH <500 m.

3.2. Comparison of PBLH retrievals from radiosonde and lidar data

Radiosonde observations can provide both thermodynamic and dynamic structures of the PBL, whereas lidar observations primarily detect its dynamic features. The potential temperature profile method and the bulk Richardson number method are thus employed to retrieve PBLH for radiosonde observations, while a TKEDR-based threshold method is employed for lidar observations. To objectively evaluate the consistency of retrieved PBLH from different observational platforms by different retrieving methods, the PBLH values observed from radiosonde and lidar are compared. Given enough valid samples of PBLH jointly detected by lidar and radiosonde, it is feasible to compare the detected PBLH between radiosonde and lidar according to the classification of PBL thermal structures. Considering that radiosonde observations are only available at 08:00 and 20:00 (BJT), during which convective development is generally weak and typical CBL is rare, the comparison between radiosonde and lidar thus focuses solely on NBL and SBL.

Here, we compare the PBLH retrieved from radiosonde (via the potential temperature profile method) and that derived from lidar (via the TKEDR-based threshold method). Under NBL conditions (Fig. 4a and Fig. S4b), the PBLH detected by the two observational platforms show a statistically significant positive correlation ($R = 0.51$, $P < 0.01$), with an RMSE of 342.46 m, indicating a generally consistent performance. Further analysis reveals several outlier cases where the difference between the two datasets is obvious (e.g., one dataset reports PBLH >1000 m, while the other <500 m, marked by triangles in Fig. 4a). To elucidate the obvious discrepancies, the potential temperature profiles observed by radiosonde and the daily TKEDR variation profiles derived by lidar corresponded to the seven triangle-marked are investigated and shown in Fig. S7.

Based on the analysis of Fig. S7, the discrepancies between radiosonde-derived and lidar-derived PBLH can be attributed to three causes. In Fig. S7a, the potential temperature profile indicates a strongly stable layer below 500 m, while the atmosphere between 500 m and 1500 m is well mixed, exhibiting typical characteristics of the planetary boundary layer, which suggests that the true PBLH lies above 1500 m. However, due to the presence of the stable layer near the surface, the potential temperature profile method misinterprets the thermal structure and underestimates the true PBLH. In Fig. S7b, the discrepancy is likely attributable to cloud development in the evening, which caused a sharp drop in the PBLH detected by lidar. In Fig. S7c-g, the primary issue is that the insufficient vertical observations of potential temperature by radiosonde prevent the detection of subtle but crucial gradients within key altitude intervals, thereby leading to inaccurate PBLH estimates. After removing these obviously deviating points (marked by triangles in Fig. 4a), as shown in Fig. 4b and Fig. S4b, under NBL conditions, the correlation increases to 0.59 with $P < 0.01$, and the RMSE decreases to 304.23 m. The mean PBLH value detected from radiosonde is 427 m, whereas that detected from lidar is 436 m, which are almost the same. By contrast, under SBL conditions (Fig. 4c and Fig. S4c), the correlation between the two observational platforms is weak and non-significant negative. This difference is likely due to the underdeveloped structure of the boundary layer during SBL periods, which is often accompanied by a strong surface temperature inversion and residual layers (Su et al.,

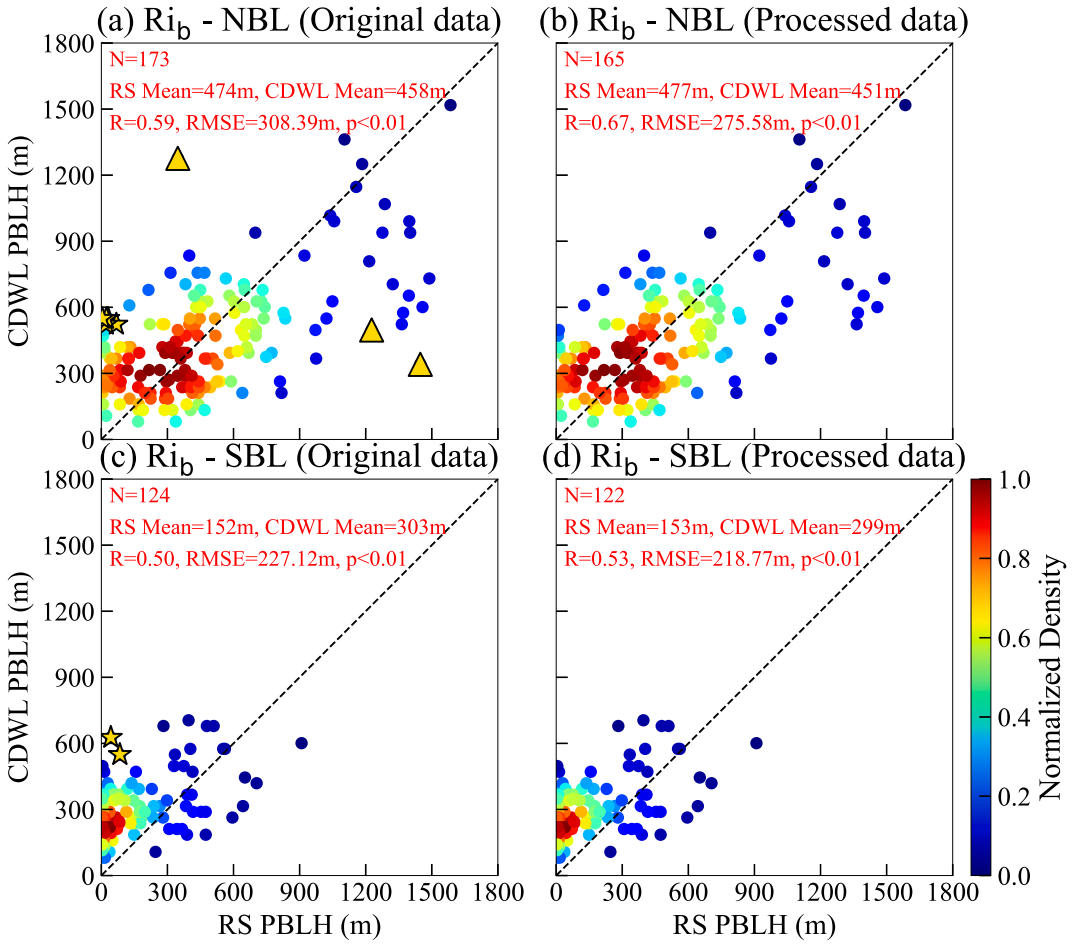

Fig. 5. Comparison of PBLH detected from radiosonde (retrieved by the bulk Richardson number method) and lidar data (retrieved by the TKEDR-based threshold method). The triangular markers indicate cases where one platform detected a PBLH >1000 m, while the other detected a PBLH <500 m. The star-shaped markers indicate cases where one platform detected a PBLH >500 m, while the other detected a PBLH <100 m.

2020). Moreover, the presence of residual layers above the SBL can affect the determination of the PBLH based on thermal structure, introducing additional uncertainty in the retrieval results (von Engeln and Teixeira, 2013). Additionally, the height of the SBL is mainly influenced by wind speed and wind shear (Che and Zhao, 2021), which are not considered in the potential temperature profile method, further contributing to retrieval errors.

Fig. 5 and Fig. S4g-h compare the PBLH retrieved from radiosonde using the bulk Richardson number method with that derived from lidar using the TKEDR-based threshold method. Under both SBL and NBL conditions, the two platforms show relatively high consistency in PBLH retrievals. Specifically, under NBL conditions, the correlation coefficient reaches 0.59 with P value < 0.01, and the RMSE is 308.39 m; under SBL conditions, the correlation coefficient is 0.50 with P value < 0.01, and the RMSE is 227.12 m. Moreover, when the radiosonde-derived PBLH is obtained using the bulk Richardson number method, the agreement with lidar remains strong under SBL conditions. This further supports the notion that the SBL is primarily influenced by wind speed and wind shear, which are not accounted for in the potential temperature profile method and thus contribute to retrieval discrepancies. Further analysis reveals some outlier cases where the difference between the two datasets is obvious (marked by triangles and stars in Fig. 5a and Fig. 5c). To elucidate the obvious discrepancies, the potential temperature profiles observed by radiosonde and the daily TKEDR variation profiles derived by lidar corresponded to the ten triangle-marked and star-marked are investigated and shown in Fig. S8.

Based on these profiles, the discrepancies between radiosonde-derived and lidar-derived PBLH in Fig. S8 can be attributed to three distinct factors. In Fig. S8a, the observation corresponds to the same time as Fig. S7a, and the discrepancy arises from the same reason discussed earlier, i.e., the presence of the stable layer near the surface, the bulk Richardson number method also underestimating the PBLH. In Fig. S8b and Fig. S8c, the discrepancies arise from the same problem in Fig. S7c-g, the insufficient vertical observations of radiosonde data fail to detect Richardson number values exceeding the 0.25 threshold within critical altitude ranges, leading to incorrect identification of the PBLH. In Fig. S8d-j, the discrepancies primarily result from uncertainties in low-level wind measurements. To be specific, the lidar is unable to observe the lowest 55 m due to its near-surface blind zone, while the radiosonde balloon often undergoes pendulum-like motion shortly after launch, introducing considerable errors in wind speed measurements near the surface (Kumer et al., 2014). Given that the Richardson number calculation is highly sensitive to wind shear, especially in the lower boundary layer, such inaccuracies can easily lead to incorrect identification of the PBLH, as previously discussed in Section 3.1 (Zhang et al., 2020a). After removing these outliers, as shown in Fig. 5b, Fig. 5d and Fig. S4g-h, the agreement of PBLH detected by the two platforms is enhanced appreciably under both NBL and SBL conditions. For NBL cases (Fig. 5b and Fig. S4g), the correlation coefficient increases to 0.67 with P value <0.01 and the RMSE decreases to 275.58 m. The mean PBLH detected from radiosonde is 477 m, while that detected from lidar is 451 m, indicating that PBLH values detected from radiosonde and lidar are highly consistent. When under SBL conditions (Fig. 5d and Fig. S4h), the correlation coefficient improves to 0.53 with P value <0.01 with an RMSE of 218.77 m. The mean PBLH value detected from radiosonde is 153 m, while that detected from lidar is 299 m, suggesting the uncertainties and bias under stable conditions are more significant than those under neutral conditions.

Furthermore, when the radiosonde PBLH is derived using the bulk Richardson number method, the consistency of the two platforms is notably better than that when the radiosonde PBLH is derived using the potential temperature profile method. This improvement may be attributed to the similarity between the physical bases of the two methods, i.e., lidar-derived PBLH is determined based on the threshold of TKEDR, which is calculated from wind speed and reflects turbulence generated by shear. Therefore, the TKEDR-based threshold method shares stronger physical consistency with the bulk Richardson number method, which also incorporates the effects of wind shear in its formula (Vickers and Mahrt, 2004). Overall, the PBLH detected from radiosonde and lidar demonstrate remarkable consistency despite using different algorithms, thereby confirming the reliability of PBLH intercomparisons derived from different observational platforms by different retrieval algorithms.

3.3. Comparison of PBLH retrievals from AMDAR and lidar data

Although we have demonstrated that PBLH values detected from different observational platforms by different retrieval methods are highly consistent, radiosonde observations are available only at 08:00 and 20:00 (BJT) and thus cannot capture the daytime evolution of the PBL. However, the daytime evolutions of PBL are very important for aviation safety and economic activities in the low-altitude airspace. In contrast, AMDAR provides numerous daytime observations, with the data volume during daytime reaching up to four times that observed at night (Moninger et al., 2003). Therefore, we further compare AMDAR and lidar observations to evaluate how well AMDAR observations characterize the thermodynamic and dynamic structures of PBL during daytime period, especially under convective conditions. Given that stable conditions seldom occur during daytime, SBL is not considered in this comparison.

In Fig. 6 and Fig. S4d-e, we illustrate the comparison between PBLH derived from AMDAR (via the potential temperature profile method) and that detected by lidar (via the TKEDR-based threshold method). Under NBL conditions, the correlation coefficient reaches 0.63 with P value < 0.01, and the RMSE is 376.45 m; under CBL conditions, the correlation coefficient is 0.69 with P value < 0.01, and the RMSE is 419.92 m. Further analysis reveals some outlier cases where the difference between the two datasets is obvious (marked by triangles and stars in Fig. 6a and Fig. 6c). To elucidate the obvious discrepancies, the potential temperature profiles observed by aircrafts and the daily TKEDR variation profiles derived by lidar corresponded to the eleven triangle-marked are investigated and shown in Fig. S9.

Based on these profiles, the discrepancies between AMDAR-derived and lidar-derived PBLH in Fig. S9 can be attributed to five distinct factors. In Fig. S9a-e, the discrepancies between the two platforms are primarily attributed to the insufficient vertical observations of potential temperature by aircrafts. In Fig. S9f, the major factor contributing to the discrepancy is temporal mismatch between the two datasets, i.e., the lidar recording PBLH at a specific and precise time, while each AMDAR data point timestamped as, for instance, 08:00, in fact reflecting atmospheric conditions observed over a broader time window (from 08:00 to 08:59). During periods of rapid PBL development, this temporal discrepancy can lead to substantial errors in PBLH comparison. In Fig. S9g and Fig. S9h, the discrepancies may result from the potential temperature profile method for identifying PBLH sometimes may misclassify CBL as NBL, leading to an underestimation of the true PBLH. In addition, the method detecting PBLH by potential temperature profile sometimes may also fail to identify the mixed layer that overlies a stable layer, thereby underestimating the PBLH (Fig. S9i and Fig. S9j). In Fig. S9k, the discrepancy is likely due to the presence of a low-level wind shear that could cause the lidar-derived PBLH to increase sharply, while the potential temperature profile method does not account for the influence of wind shear. After excluding these outliers, as illustrated in Fig. 6b, Fig. 6d and Fig. S4d-e, the consistency in PBLH detection between the two platforms improves notably. The correlation coefficient reaches 0.71 ($P < 0.01$) with an RMSE of 330.26 m for NBL cases

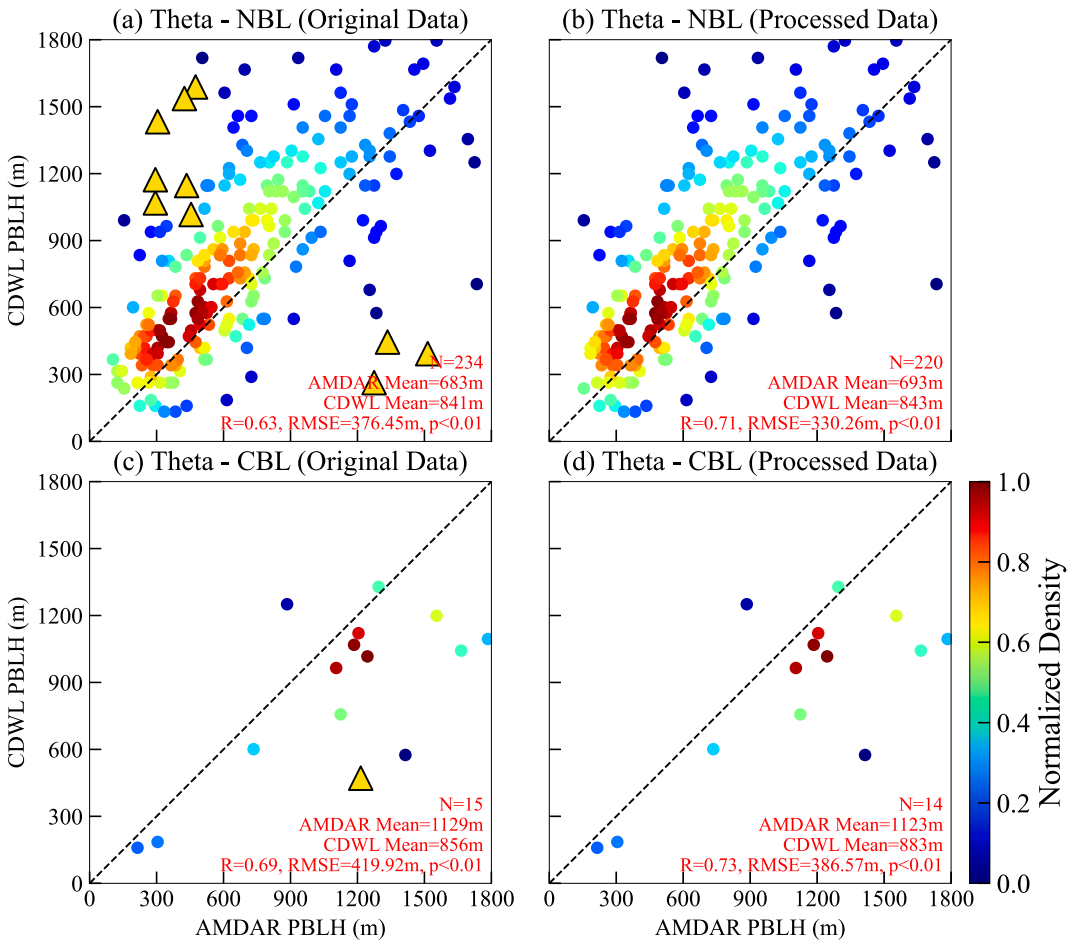

Fig. 6. Comparison of PBLH detected from AMDAR (retrieved by the potential temperature profile method) and lidar data (retrieved by the TKEDR-based threshold method). The triangular markers indicate cases where one platform detected a PBLH >1000 m, while the other detected a PBLH <500 m.

(Fig. 6b) and 0.73 (P < 0.01) with an RMSE of 386.57 m for CBL cases (Fig. 6d). Under NBL conditions, the mean PBLH value detected from AMDAR is 693 m, while that detected from lidar is 843 m, indicating that the AMDAR's observations of PBLH tend to be lower than lidar. However, when the PBL is under convective conditions, the mean PBLH value detected from AMDAR is 1123 m, whereas that detected from lidar is 883 m.

When the bulk Richardson number method is applied to AMDAR data for PBLH retrieval, the comparison with lidar-derived PBLH shows significant consistency, as illustrated in Fig. 7 and Fig. S4i-j. Under NBL and CBL conditions, the correlation coefficients are 0.49 ($P < 0.01$) with an RMSE of 422.45 m (Fig. 7a) and 0.59 ($P < 0.05$) with an RMSE of 406.44 m (Fig. 7c), respectively. Further analysis reveals some outlier cases for NBL conditions where the difference between the two datasets is obvious (marked by triangles and stars in Fig. 7a). To elucidate the obvious discrepancies, the potential temperature profiles observed by aircrafts and the daily TKEDR variation profiles derived by lidar corresponded to the nineteen triangle-marked and star-marked are investigated and shown in Fig. S10. Based on these profiles, the discrepancies between AMDAR-derived and lidar-derived PBLH in Fig. S10 can be attributed to two factors. In Fig. S10a-g, the discrepancies between the two detecting platforms are primarily attributed to the sparse vertical observations of airplanes. The deviations observed in Fig. S10h-s are predominantly attributed to relatively stronger vertical variations in wind speed within the lower boundary layer than the corresponding potential temperature. Given the high sensitivity of the bulk Richardson number method to wind observations, inadequate wind data under these conditions may lead to substantial errors in PBLH retrieval. After excluding these outliers, as illustrated in Fig. 7b and Fig. S4i, the consistency in PBLH detection between the two platforms improves notably. The correlation coefficient reaches 0.67 (P < 0.01) with an RMSE of 324.77 m. Under NBL conditions, the mean PBLH value detected from AMDAR is 769 m, while that detected from lidar is 794 m. However, under CBL conditions, the mean PBLH value detected from AMDAR is 1110 m, notably larger than that detected from lidar (865 m). This difference is consistent with the result derived from the potential temperature profile method.

Conspicuously, the potential temperature profile method applied to AMDAR data yields a stronger and more statistically significant correlation with the lidar-derived PBLH compared to the bulk Richardson number method. This may be attributed to the relatively low vertical resolution of aircraft measurements, which limits the accuracy of the bulk Richardson number method due to its higher sensitivity to wind field (Zhang et al., 2020a). Overall, AMDAR exhibits a strong capability in capturing thermodynamic and dynamic structures of daytime CBL.

3.4. *Integrated observations for continuous PBLH monitoring*

Overall, the PBLH detected by radiosonde, lidar, and AMDAR data all exhibit high accuracy. Therefore, the observations of lidar, radiosonde, and AMDAR are integrated to detect PBLH, so as to obtain the effective full-day PBLH. To visually exhibit the diurnal and seasonal evolutions of PBLH, the diurnal variations of PBLH detected from the three observational platforms on representative days during spring, summer, autumn, and winter, as well as the boxplots of average PBLH diurnal variation during different seasons, are shown in Fig. 8. Winter is excluded from

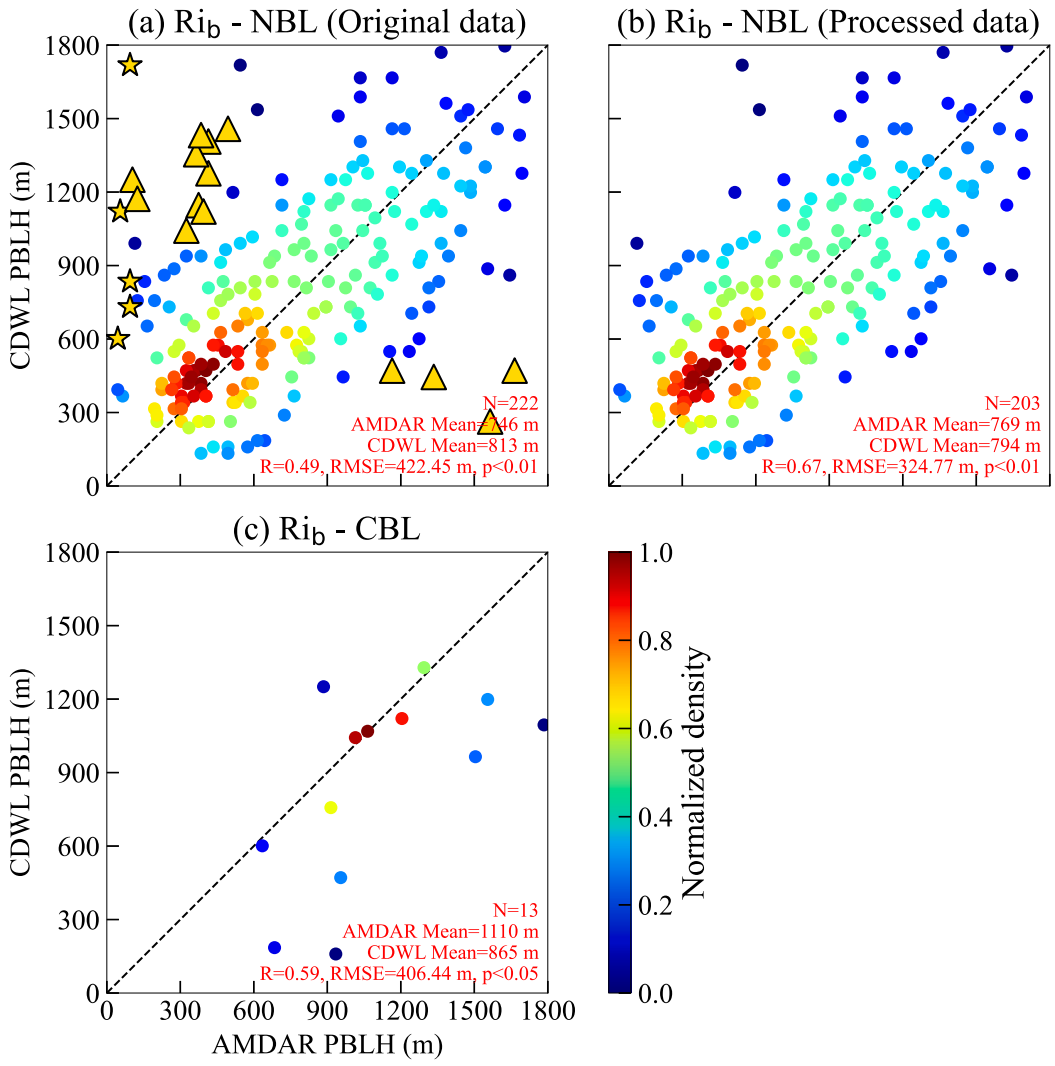

Fig. 7. Comparison of PBLH detected from AMDAR (retrieved by the bulk Richardson number method) and lidar data (retrieved by the TKEDR-based threshold method). The triangular markers indicate cases where one platform detected a PBLH >1000 m, while the other detected a PBLH <500 m. The star-shaped markers indicate cases where one platform detected a PBLH >500 m, while the other detected a PBLH <100 m.

the boxplot analysis due to the limited number of available samples (only December of 2022).

As shown in Fig. 8, lidar measurements, with high temporal and vertical resolution, can effectively capture the continuous and subtle variations of the PBLH throughout the day. Radiosonde data, despite being limited to fixed launch times at 08:00 and 20:00 (BJT), provide accurate vertical profiles and remain essential for characterizing stable or neutral boundary layer structure. With relatively frequent availability during daytime hours, AMDAR data serves as a useful supplement to bridge the temporal gap between radiosonde's observations, thereby enhancing continuous monitoring of PBLH over the daytime periods, especially for the convective boundary layer structure (Fig. 8a, Fig. 8c, Fig. e and Fig. 8f). By integrating these complementary datasets, the limitations inherent in each individual observation method can be mitigated. This multi-platform approach provides a more comprehensive and accurate characterization of PBLH, thereby enabling full-day monitoring of PBLH. The full-day evolutions of PBLH are shown in Fig. 8a-g and we can find that PBLH is shallow overnight, grows after sunrise, and typically rises to a peak in the afternoon between 14:00 to 15:00 (BJT). Additionally, it is evident that the daytime PBLH values during spring and summer (Fig. 8a–d) are markedly higher than those during autumn and winter (Fig. 8e–g), consistent with previous findings (Miao et al., 2015; Tang et al., 2016). Compared with daytime PBLH, the seasonal differences in nighttime or early morning PBLH are much smaller as the boundary layers during nighttime or early morning of all seasons are relatively shallow.

4. Conclusion and discussion

This study comprehensively evaluates the performances of PBLH retrieval using three observational platforms i.e., radiosonde, AMDAR, and lidar. Firstly, the PBLH detected from both radiosonde and AMDAR observations is based on two methods i.e., the potential temperature profile method and the bulk Richardson number method, while the PBLH detected from lidar observation is only based on one method i.e., the TKEDR-based threshold method. Then, we evaluate the performances of the above detected PBLH that is stratified by SBL, NBL, and CBL and examine the underlying causes of the substantial discrepancies in PBLH among the three observational platforms. Finally, the PBLH detected from the lidar, radiosonde, and AMDAR observations are integrated to effectively monitor the full-day PBLH.

All three observational platforms exhibit promising capability in PBLH retrieval. However, the performance of retrieval methods varies with the boundary layer types and observing platforms. Under SBL conditions, since the height of the SBL is mainly influenced by wind speed and wind shear (Che and Zhao, 2021), the potential temperature

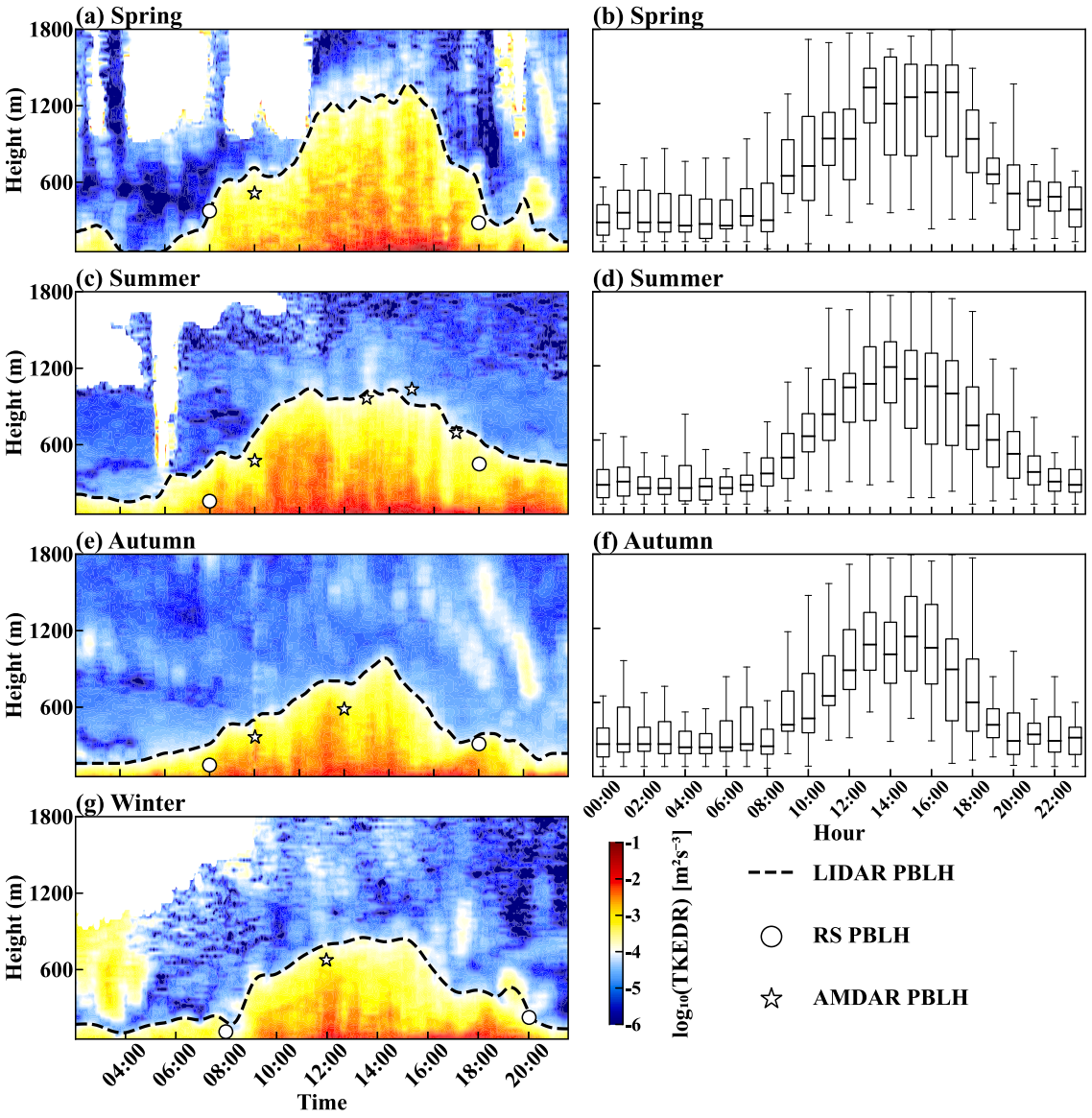

Fig. 8. Diurnal variations of PBLH detected from integrated observations of lidar, radiosonde, and AMDAR. The single-day PBLH variations during spring, summer, autumn, and winter are respectively shown in (a), (c), (e), and (g). The average seasonal diurnal variations of PBLH during spring, summer, and autumn are respectively shown in (b), (d), and (f).

profile method showed limited accuracy, while the bulk Richardson number method is proved to be more suitable. For NBL and CBL, both methods performed better, with higher consistency observed compared to SBL. When comparing PBLH retrieved from radiosonde with that from lidar, the bulk Richardson number method produces better agreement than the potential temperature profile method. This is because the bulk Richardson number method shares stronger physical consistency with the TKEDR-based threshold method used for lidar, as both account for wind shear and turbulence effects (Vickers and Mahrt, 2004). In contrast, when comparing PBLH observed from AMDAR with lidar or radiosonde, the potential temperature profile method outperforms the bulk Richardson number method. This outcome reflects the relatively low vertical resolution of aircraft measurements, which cannot adequately capture wind field variations, but the bulk Richardson number method is highly sensitive to wind shear (Zhang et al., 2020a). In addition, the PBLH detected by radiosonde, AMDAR, and lidar observations are integrated to monitor full-day PBLH, especially compensating for the radiosonde's limited ability to monitor the daytime convective boundary layer.

The major innovation of this study is that we comprehensively and systematically evaluate the PBL characteristics detected from three observational platforms i.e., radiosonde, AMDAR, and lidar, over Beijing, China, with the aim of monitoring full-day evolution of PBL by integrating observations from these platforms. Our results highlight the PBLH and thermal structure of the PBL derived from AMDAR observations over Beijing, China are reliable and highly accurate, exhibiting strong consistency with AMDAR-detect PBL features over the United States and eastern China (Ding et al., 2015; Ding et al., 2018; Zhang et al., 2020b; Xu et al., 2022; Ayazpour et al., 2023). Unlike previous work, the underlying causes of obvious discrepancies between AMDAR-derived PBL and those from radiosonde or lidar are also examined in our study and the performance of AMDAR detecting PBL is markedly enhanced by eliminating these outliers with large discrepancies, which can provide a new insight for employing AMDAR data in PBL research and applications. In addition, we also comprehensively analyze PBL features from radiosonde, AMDAR, and lidar to monitor full-day evolutions of PBL, which is essential for advancing our understanding of PBL and improving numerical forecasting.

Our results demonstrated the reliability of AMDAR data for detecting PBLH and the thermal structure of PBL. The meteorological vertical profile datasets observed by aircrafts at a large number of airports in the United States and Europe are publicly released online and thus provide high-resolution spatiotemporal datasets for detecting vertical structures of atmosphere (Schwartz and Benjamin, 1995; Benjamin et al., 1999; Drüe et al., 2010; Petersen et al., 2016; Zhang et al., 2019). However, only a few megacities in China such as Beijing, Hong Kong and so on, with flights to the United States and Europe, share the meteorological datasets (Lv et al., 2020; Ng and Hon, 2022) and the observations from commercial aircraft flying domestic routes within China remain unavailable to the public. Notably, the low-altitude air space opening policy had been implemented by the Chinese government and the flight activities within the PBL below 1000 m have increased significantly (Fan et al., 2017). Meanwhile, the demand for meteorological support to ensure low-altitude flight safety is becoming increasingly prominent, in particular for the high-resolution spatiotemporal structures of PBL. Therefore, the meteorological profile datasets such as temperature, horizontal wind vector, pressure, and turbulence observed by the domestic commercial aircraft over China urgently need to be made accessible for researchers to enhance research on the thermodynamic and dynamic structural changes within PBL, thereby improving meteorological service capabilities for the low-altitude economy.

CRediT authorship contribution statement

Jieyu Hou: Writing – original draft, Visualization, Methodology, Formal analysis, Data curation. **Mengyao Li:** Writing – review & editing, Data curation. **Guicai Ning:** Writing – review & editing, Validation, Supervision, Resources, Methodology, Conceptualization. **Tianwen Wei:** Methodology, Formal analysis, Data curation. **Jinlong Yuan:** Methodology, Formal analysis. **Haiyun Xia:** Validation, Supervision, Resources.

Declaration of competing interest

The authors declare that they have no known competing financial interests or personal relationships that could have appeared to influence the work reported in this paper.

Acknowledgements

The appointment of Guicai Ning at Nanjing University of Information Science & Technology is partially supported by the Jiangsu Specially-Appointed Professor (grant no. R2023T01). This study is also funded by the project CPUME202403 that was supported by Chengdu Plain Urban Meteorology and Environment Observation and Research Station of Sichuan Province (grant no. CPUME202403). The authors thank Met Office and NOAA for providing AMDAR data, the lab of Haiyun Xia at the Nanjing University of Information Science & Technology for providing lidar data, and the University of Wyoming for providing Beijing radiosonde data. The authors are thankful to the High Performance Computing Center of Nanjing University of Information Science & Technology for their support of this work. The authors also thank Dr. Yuanjie Zhang at the Nanjing University of Information Science & Technology for helpful discussions.

Appendix A. Supplementary data

Supplementary data to this article can be found online at https://doi.org/10.1016/j.atmosres.2025.108701.

Data availability

The radiosonde dataset used in this study is obtained from the University of Wyoming Atmospheric Science Radiosonde Archive at https://weather.uwyo.edu/upperair/sounding.html. The AMDAR data used in this study are available through the Meteorological Assimilation Data Ingest System web service portal at https://madis-data.cprk.ncep.noaa.gov/madisPublic1/ (last access: 10 August 2025; NOAA, 2025) and Met Office web service portal at https://catalogue.ceda.ac.uk/uuid/33f44351f9ceb09c495b8cef74860726 (last access: 10 August 2025; Met Office, 2008). The surface meteorological data can be found at https://www.ncei.noaa.gov/metadata/geoportal/rest/metadata/item/gov.noaa.ncdc:C00532/html# (last access: 10 August 2025; NOAA National Centers for Environmental Information, 2001). The Doppler wind lidar data used in this study can be provided for non-commercial research purposes upon request to the first author (Jieyu Hou, 202283110002@nuist.edu.cn).

References

Ayazpour, Z., Tao, S., Li, D., Scarino, A.J., Kuehn, R.E., Sun, K., 2023. Estimates of the spatially complete, observational-data-driven planetary boundary layer height over the contiguous United States. Atmos. Meas. Tech. 16, 563–580. https://doi.org/10.5194/amt-16-563-2023.

Banakh, V.A., Smalikho, I.N., Falits, A.V., 2021. Estimation of the height of the turbulent mixing layer from data of Doppler lidar measurements using conical scanning by a probe beam. Atmos. Meas. Tech. 14, 1511–1524. https://doi.org/10.5194/amt-14-1511-2021.

Benjamin, S.G., Schwartz, B.E., Cole, R.E., 1999. Accuracy of ACARS wind and temperature observations determined by collocation wea. Forecasting 14, 1032–1038. https://doi.org/10.1175/1520-0434(1999)014<1032:AOAWAT>2.0.CO;2.

Canché-Cab, L., San-Pedro, L., Ali, B., Rivero, M., Escalante, M., 2024. The atmospheric boundary layer: a review of current challenges and a new generation of machine learning techniques. Artif. Intell. Rev. 57, 331. https://doi.org/10.1007/s10462-024-10962-5.

Che, J., Zhao, P., 2021. Characteristics of the summer atmospheric boundary layer height over the Tibetan Plateau and influential factors. Atmos. Chem. Phys. 21, 5253–5268. https://doi.org/10.5194/acp-21-5253-2021.

Chen, Y., Jin, X., Weng, N., Zhu, W., Liu, Q., Chen, J., 2022. Simultaneous extraction of planetary boundary-layer height and aerosol optical properties from coherent doppler wind lidar. Sensors 22, 3412. https://doi.org/10.3390/s22093412.

Cooper, D.I., Eichinger, W.E., 1994. Structure of the atmosphere in an urban planetary boundary layer from lidar and radiosonde observations. J. Geophys. Res.-Atmos. 99, 22937–22948. https://doi.org/10.1029/94JD01944.

Ding, J., Zhuge, X.-Y., Wang, Y., Xiong, A., 2015. Evaluation of chinese aircraft meteorological data relay (AMDAR) weather reports. J. Atmos. Oceanic Tech. 32, 982–992. https://doi.org/10.1175/JTECH-D-14-00145.1.

Ding, J., Zhuge, X., Li, X., Yuan, Z., Wang, Y., 2018. Evaluation of accuracy of Chinese AMDAR data for 2015. J. Atmos. Oceanic Tech. 35, 943–951. https://doi.org/10.1175/JTECH-D-17-0095.1.

Doerenbecher, A., Mahfouf, J.F., 2019. Impact of additional AMDAR data in the AROME-France model during May 2017. Adv. Sci. Res. 16, 215–222. https://doi.org/10.5194/asr-16-215-2019.

Drüe, C., Hauf, T., Hoff, A., 2010. Comparison of boundary-layer profiles and layer detection by AMDAR and WTR/RASS at Frankfurt airport. Bound.-Lay. Meteorol. 135, 407–432. https://doi.org/10.1007/s10546-010-9485-0.

Fan, Q., Zhu, K., Zheng, J., Zhang, J., Zhou, D., Zhang, F., 2017. Detection performance analysis of all-fiber coherent wind lidar under different weather types. Chin. J. Lasers 44, 320–329. https://doi.org/10.3788/CJL201744.0210003.

Garratt, J.R., 1994. Review: the atmospheric boundary layer. Earth Sci. Rev. 37, 89–134. https://doi.org/10.1016/0012-8252(94)90026-4.

Guo, J., Miao, Y., Zhang, Y., Liu, H., Li, Z., Zhang, W., He, J., Lou, M., Yan, Y., Bian, L., Zhai, P., 2016. The climatology of planetary boundary layer height in China derived from radiosonde and reanalysis data. Atmos. Chem. Phys. 16, 13309–13319. https://doi.org/10.5194/acp-16-13309-2016.

Hanna, S.R., 1969. The thickness of the planetary boundary layer. Atmos. Environ. 1967-1989 (3), 519–536. https://doi.org/10.1016/0004-6981(69)90042-0.

Kumer, V.-M., Reuder, J., Furevik, B.R., 2014. A Comparison of LiDAR and Radiosonde Wind Measurements. Energy Procedia 53, 214–220. https://doi.org/10.1016/j.egypro.2014.07.230.

Li, H., Liu, B., Ma, X., Jin, S., Ma, Y., Zhao, Y., Gong, W., 2021. Evaluation of retrieval methods for planetary boundary layer height based on radiosonde data. Atmos. Meas. Tech. 14, 5977–5986. https://doi.org/10.5194/amt-14-5977-2021.

Liu, S., Liang, X.-Z., 2010. Observed diurnal cycle climatology of planetary boundary layer height. J. Climate 23, 5790–5809. https://doi.org/10.1175/2010JCLI3552.1.

Lv, Z., Wei, W., Cheng, S., Han, X., Wang, X., 2020. Mixing layer height estimated from AMDAR and its relationship with PMs and meteorological parameters in two cities in North China during 2014–2017. Atmos. Pollut. Res. 11, 443–453. https://doi.org/10.1016/j.apr.2019.11.017.

Miao, Y., Liu, S., 2019. Linkages between aerosol pollution and planetary boundary layer structure in China. Sci. Total Environ. 650, 288–296. https://doi.org/10.1016/j.scitotenv.2018.09.032.

Miao, Y., Hu, X.-M., Liu, S., Qian, T., Xue, M., Zheng, Y., Wang, S., 2015. Seasonal variation of local atmospheric circulations and boundary layer structure in the

Beijing-Tianjin-Hebei region and implications for air quality, 7, pp. 1602–1626. https://doi.org/10.1002/2015MS000522.
Milroy, C., Martucci, G., Lolli, S., Loaec, S., Sauvage, L., Xueref-Remy, I., Lavrič, J.V., Ciais, P., Feist, D.G., Biavati, G., O'Dowd, C.D., 2012. An assessment of pseudo-operational ground-based light detection and ranging sensors to determine the boundary-layer structure in the coastal atmosphere. Adv. Meteorol. 929080. https://doi.org/10.1155/2012/929080.
Moninger, W.R., Mamrosh, R.D., Pauley, P.M., 2003. Automated meteorological reports from commercial aircraft bull. Amer. Meteor. Soc. 84, 203–216. https://doi.org/10.1175/BAMS-84-2-203.
Ng, C.W., Hon, K.K., 2022. Fast dual-doppler LiDAR retrieval of boundary layer wind profiles. Weather 77, 134–142. https://doi.org/10.1002/wea.3800.
Petersen, R.A., Cronce, L., Mamrosh, R., Baker, R., Pauley, P., 2016. On the impact and future benefits of AMDAR observations in operational forecasting: part II: water vapor observations bull. Amer. Meteor. Soc. 97, 2117–2133. https://doi.org/10.1175/BAMS-D-14-00211.1.
Quan, J., Gao, Y., Zhang, Q., Tie, X., Cao, J., Han, S., Meng, J., Chen, P., Zhao, D., 2013. Evolution of planetary boundary layer under different weather conditions, and its impact on aerosol concentrations. Particuology 11, 34–40. https://doi.org/10.1016/j.partic.2012.04.005.
Rahn, D.A., Mitchell, C.J., 2016. Diurnal climatology of the boundary layer in Southern California using AMDAR temperature and wind profiles. J. Appl. Meteorol. Clim. 55, 1123–1137. https://doi.org/10.1175/JAMC-D-15-0234.1.
Richardson, H., Basu, S., Holtslag, A.A.M., 2013. Improving stable boundary-layer height estimation using a stability-dependent critical bulk Richardson number. Bound.-Lay. Meteorol. 148, 93–109. https://doi.org/10.1007/s10546-013-9812-3.
Schwartz, B., Benjamin, S.G., 1995. A comparison of temperature and wind measurements from ACARS-equipped aircraft and rawinsondes wea. Forecasting 10, 528–544. https://doi.org/10.1175/1520-0434(1995)010<0528:ACOTAW>2.0.CO;2.
Seidel, D.J., Ao, C.O., Li, K., 2010. Estimating climatological planetary boundary layer heights from radiosonde observations: Comparison of methods and uncertainty analysis. J. Geophys. Res.-Atmos. 115. https://doi.org/10.1029/2009JD013680.
Seidel, D.J., Zhang, Y., Beljaars, A., Golaz, J.-C., Jacobson, A.R., Medeiros, B., 2012. Climatology of the planetary boundary layer over the continental United States and Europe. J. Geophys. Res.-Atmos. 117. https://doi.org/10.1029/2012JD018143.
Shao, N., Lu, C., Jia, X., Wang, Y., Li, Y., Yin, Y., Zhu, B., Zhao, T., Liu, D., Niu, S., Fan, S., Yan, S., Lv, J., 2023. Radiation fog properties in two consecutive events under polluted and clean conditions in the Yangtze River Delta, China: a simulation study. Atmos. Chem. Phys. 23, 9873–9890. https://doi.org/10.5194/acp-23-9873-2023.
Smalikho, I.N., Banakh, V.A., 2017. Measurements of wind turbulence parameters by a conically scanning coherent Doppler lidar in the atmospheric boundary layer. Atmos. Meas. Tech. 10, 4191–4208. https://doi.org/10.5194/amt-10-4191-2017.
Stull, R., 1988. B.: An Introduction to Boundary Layer Meteorology. Springer, Netherlands, Dordrecht. https://doi.org/10.1007/978-94-009-3027-8, 1-27 pp.
Su, T., Li, Z., Kahn, R., 2020. A new method to retrieve the diurnal variability of planetary boundary layer height from lidar under different thermodynamic stability conditions. Remote Sens. Environ. 237, 111519. https://doi.org/10.1016/j.rse.2019.111519.
Su, L., Lu, C., Yuan, J., Wang, X., He, Q., Xia, H., 2024. Measurement report: the promotion of the low-level jet and thermal effects on the development of the deep convective boundary layer at the southern edge of the Taklimakan Desert. Atmos. Chem. Phys. 24, 10947–10963. https://doi.org/10.5194/acp-24-10947-2024.
Sun, X., 2023. Variations of PM2.5 Pollution over the Twain-Hu Basin with Interaction of Atmospheric Boundary Layer in Regional Transport of Air Pollutants. Ph.D. thesis. Nanjing University of Information Science and Technology. https://doi.org/10.27248/d.cnki.gnjqc.2023.000033.
Tang, G., Zhang, J., Zhu, X., Song, T., Münkel, C., Hu, B., Schäfer, K., Liu, Z., Zhang, J., Wang, L., Xin, J., Suppan, P., Wang, Y., 2016. Mixing layer height and its implications for air pollution over Beijing, China. Atmos. Chem. Phys. 16, 2459–2475. https://doi.org/10.5194/acp-16-2459-2016.
Vickers, D., Mahrt, L., 2004. Evaluating Formulations of Stable Boundary Layer Height. J. Appl. Meteor. Climatol. 43, 1736–1749. https://doi.org/10.1175/JAM2160.1.
von Engeln, A., Teixeira, J., 2013. A planetary boundary layer height climatology derived from ECMWF reanalysis data. J. Climate 26, 6575–6590. https://doi.org/10.1175/JCLI-D-12-00385.1.
Wang, L., 2022. Retrieval and Analysis of Atmospheric Boundary Layer Height Based on Turbulent Kinetic Energy Dissipation Rate. Ph.D. thesis. University of Science and Technology of China. https://doi.org/10.27517/d.cnki.gzkju.2022.000448.
Wang, Z., Li, J., Zhong, Z., Liu, D., Zhou, J., 2008. LIDAR exploration of atmospheric boundary layer over downtown of Beijing in summer. J. Appl. Opt. 29, 96–100.
Wang, C., Shi, H., Jin, L., Chen, H., Wen, H., 2016. Measuring boundary-layer height under clear and cloudy conditions using three instruments. Particuology 28, 15–21. https://doi.org/10.1016/j.partic.2015.04.004.
Wang, L., Qiang, W., Xia, H., Wei, T., Yuan, J., Jiang, P., 2021. Robust solution for Boundary Layer Height Detections with Coherent Doppler Wind Lidar. Adv. Atmos. Sci. 38, 1920–1928. https://doi.org/10.1007/s00376-021-1068-0.
Wang, M., Wei, T., Lolli, S., Wu, K., Wang, Y., Hu, H., Yuan, J., Tang, D., and Xia, H.: A long-term doppler wind LiDAR study of heavy pollution episodes in western Yangtze River Delta region, China, Atmos. Res., 310, 107616, https://doi.org/10.1016/j.atmosres.2024.107616, 2024aa.
Wang, Y., Yi, N., Jiang, X., Ning, G., Su, L., and Xia, H.: Diagnosis of severe dust weather process based on multi-source observational data, J. Desert Res., 44, 195–206, https://doi.org/10.7522/j.issn.1000-694X.2024.00075, 2024bb.
Wang, L., He, F., Yuan, J., Hu, G., Mei, J., Han, S., Hong, L., Xia, H., 2025. A robust threshold method of mixed layer height based on lidar turbulence data under different thermal convection conditions. Bound.-Lay. Meteorol. 191, 32. https://doi.org/10.1007/s10546-025-00918-9.
Xu, X., Zhang, Y., Song, S., Yang, Y., Li, X., Gao, Z., 2022. Evaluation and application of atmospheric boundary layer profiles from aircraft meteorological reports in central and eastern China. Chinese J. Geophs-CH 65, 4174–4193. https://doi.org/10.6038/cjg2022P0432.
Yin, J., Gao, C.Y., Hong, J., Gao, Z., Li, Y., Li, X., Fan, S., Zhu, B., 2019. Surface meteorological conditions and boundary layer height variations during an air pollution episode in Nanjing, China. J. Geophys. Res.-Atmos. 124, 3350–3364. https://doi.org/10.1029/2018JD029848.
Zhang, Y., Seidel, D.J., Zhang, S., 2013. Trends in planetary boundary layer height over Europe. J. Climate 26, 10071–10076. https://doi.org/10.1175/JCLI-D-13-00108.1.
Zhang, Y., Gao, Z., Li, D., Li, Y., Zhang, N., Zhao, X., Chen, J., 2014. On the computation of planetary boundary-layer height using the bulk Richardson number method. Geosci. Model Dev. 7, 2599–2611. https://doi.org/10.5194/gmd-7-2599-2014.
Zhang, W., Guo, J., Miao, Y., Liu, H., Zhang, Y., Li, Z., Zhai, P., 2016. Planetary boundary layer height from CALIOP compared to radiosonde over China. Atmos. Chem. Phys. 16, 9951–9963. https://doi.org/10.5194/acp-16-9951-2016.
Zhang, Y., Li, D., Lin, Z., Santanello Jr., J.A., Gao, Z., 2019. Development and evaluation of a long-term data record of planetary boundary layer profiles from aircraft meteorological reports. J. Geophys. Res.-Atmos. 124, 2008–2030. https://doi.org/10.1029/2018JD029529.
Zhang, H., Zhang, X., Li, Q., Cai, X., Fan, S., Song, Y., Hu, F., Che, H., Quan, J., Kang, L., Zhu, T., 2020a. Research progress on estimation of the atmospheric boundary layer height. J. Meteorol. Res. 34, 482–498. https://doi.org/10.1007/s13351-020-9910-3.
Zhang, Y., Sun, K., Gao, Z., Pan, Z., Shook, M.A., Li, D., 2020b. Diurnal climatology of planetary boundary layer height over the contiguous United States derived from AMDAR and reanalysis data. J. Geophys. Res.-Atmos. 125. https://doi.org/10.1029/2020JD032803 e2020JD032803.
Zhong, T., Wang, N., Shen, X., Xiao, D., Xiang, Z., Liu, D., 2020. Determination of planetary boundary layer height with lidar signals using maximum limited height initialization and range restriction (MLHI-RR). Remote Sens. 12, 2272. https://doi.org/10.3390/rs12142272.
Zilitinkevich, S.S., 2012. The height of the atmospheric planetary boundary layer: state of the art and new development. In: National Security and Human Health Implications of Climate Change, Dordrecht, 08 October 2011. https://doi.org/10.1007/978-94-007-2430-3_13.
Zilitinkevich, S., Baklanov, A., 2002. Calculation of the height of the stable boundary layer in practical applications. Bound.-Lay. Meteorol. 105, 389–409. https://doi.org/10.1023/A:1020376832738.